A Generalized Finite Element Method for polycrystals with discontinuous grain boundaries

A. Simone[a,1], C.A. Duarte[b] and E. Van der Giessen[a]

[a] *Netherlands Institute for Metals Research / Micromechanics of Materials Group, Materials Science Center, University of Groningen*
Nyenborgh 4, 9747 AG Groningen, the Netherlands

[b] *Department of Civil and Environmental Engineering, University of Illinois at Urbana-Champaign*
2122 Newmark Laboratory MC 250, 205 North Mathews Av., Urbana, Illinois 61801, USA

SUMMARY

We present a Generalized Finite Element Method for the analysis of polycrystals with explicit treatment of grain boundaries. Grain boundaries and junctions, understood as loci of possible displacement discontinuity, are inserted into finite elements by exploiting the partition of unity property of finite element shape functions. Consequently, the finite element mesh does not need to conform to the polycrystal topology. The formulation is outlined and a numerical example is presented to demonstrate the potential and accuracy of the approach. The proposed methodology can also be used for branched and intersecting cohesive cracks, and comparisons are made to a related approach (C. Daux, N. Moës, J. Dolbow, N. Sukumar and T. Belytschko, Int. J. Numer. Meth. Engng. 48 (2000) 1741).

KEY WORDS: Generalized Finite Element Method; eXtended Finite Element Method; partition of unity; grain boundary sliding; polycrystals

1. INTRODUCTION

Finite element method analyses of polycrystals rely on the use of generators to design the mesh around the polycrystal topology [1–3], as shown for example in Figure 1. Sometimes the result is far from optimal, very difficult to improve and time consuming. The situation gets worse in a three-dimensional configuration, and there are cases, e.g. when grains are shaped like a wedge (very flat and long), in which is not even possible to achieve the desired quality.

The method that we propose does not need a mesh generator to mimic the polycrystal. It requires a simple background mesh on which the polycrystal topology is superimposed, as schematically depicted in Figure 2, and a simple key assumption on the form of the

[1] Correspondence to: A. Simone, Delft University of Technology, Faculty of Civil Engineering and Geosciences, P.O. Box 5048, 2600 GA Delft, The Netherlands
E-mail: a.simone@tudelft.nl

⋆ *International Journal for Numerical Methods in Engineering*: Submitted August 27, 2005. Revised December 12, 2005

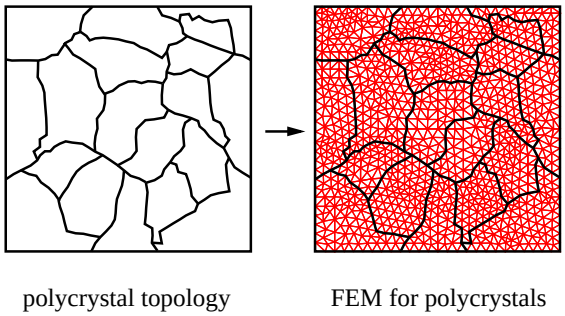

Figure 1. FEM approximation of a polycrystal sample.

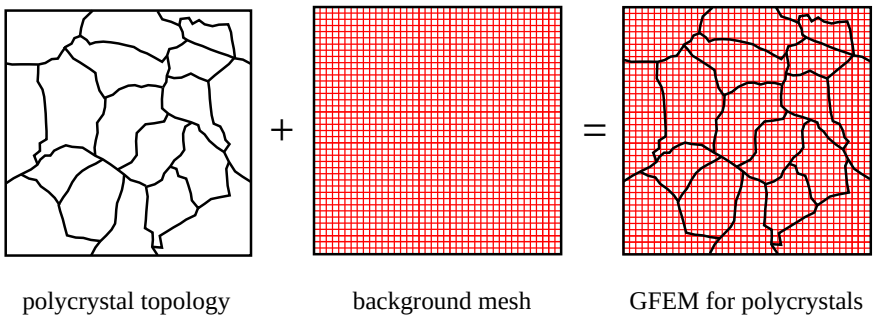

Figure 2. Proposed GFEM approximation of a polycrystal sample.

displacement field [4]. As described in Sections 2 and 3, our approach hinges on the concept of local approximations for Generalized Finite Element Methods (GFEM's) [5, 6], and relies on novel developments in the description of displacement discontinuities [4] (the construction of a GFEM discrete space parallels that of the eXtended Finite Element Method [7] and is described in Section 4).

In the GFEM for polycrystals, the grain boundaries and junctions are represented by means of elements with embedded cohesive displacement discontinuities [4, 8, 9]. There are no limitations on grain shape and the number of grain boundaries meeting at a junction, and any grain boundary behavior can be handled [10–12]. There is however a range of situations where the boundaries of grains in polycrystals have a significant influence on the overall deformation and fracture behavior. One example is grain boundary sliding [13, 14]; in Section 7, we consider a simple application on the effect of grain boundary sliding on anelasticity of polycrystals [14]. In terms of topological representations, our model capabilities are similar to those of the Voronoi cell finite element model by Ghosh [15] and the conforming polygonal finite element method by Sukumar and Tabarraei [16].

Our GFEM approximation for polycrystals, whose formulation and implementation are described in Sections 5 and 6, can also be used for branched and intersecting cohesive cracks in two or three dimensions. In Section 4, we show that our approach in 2-D produces the same approximation spaces as a technique making use of the XFEM [7]. However, the choice

of enrichment functions is simplified, thus making it an appealing alternative to the XFEM.

2. PARTITIONS OF UNITY AND FINITE ELEMENTS

In this section, we recall some basic notions on the partition of unity paradigm and its relation to finite element methods. The construction of a partition of unity can be based on the definition of *clouds* [5], which are overlapping open sets ω_α of arbitrary shape, centered at node $\boldsymbol{x}_\alpha$, covering the solution domain $\bar{\Omega}$ of a boundary value problem ($\bar{\Omega} \subset \bigcup_{\alpha=1}^{N} \bar{\omega}_\alpha$, where N is the number of nodes of the discretization; an overbar indicates the closure of a set). A *partition of unity* is defined as a collection of global functions $\varphi_\alpha(\boldsymbol{x})$ whose support is contained in a cloud and whose value sums up to unity at each point $\boldsymbol{x}$ in the solution domain:

$$\sum_{\alpha=1}^{N} \varphi_\alpha(\boldsymbol{x}) = 1 \qquad \forall \boldsymbol{x} \in \bar{\Omega}. \tag{1}$$

The FEM can be used as a framework for the construction of clouds since the support of a node can be understood as a cloud [17, 18] and Equation (1) holds by construction for any Lagrangian FEM global basis (i.e. shape function). Using linear partitions of unity φ_α as basis functions in a FEM framework [19], a scalar field $q(\boldsymbol{x})$ can be approximated by

$$q_h(\boldsymbol{x}) = \underbrace{\sum_{\alpha=1}^{N} \varphi_\alpha(\boldsymbol{x}) \hat{q}_\alpha}_{\text{regular interpolation}} + \underbrace{\sum_{\alpha=1}^{N} \varphi_\alpha(\boldsymbol{x}) \sum_{j=1}^{m} E_j(\boldsymbol{x}) \tilde{q}_{\alpha j}}_{\text{enrichment}}, \tag{2}$$

where the subscript 'h' denotes the approximate field, $\hat{q}_\alpha$ (termed 'regular' or 'standard' degrees of freedom (dofs)) are nodal values related to the basis φ_α, and $\tilde{q}_{\alpha j}$ (termed 'enrichment' or 'extra' degrees of freedom) are the global nodal parameters connected to the basis E_j pertinent to the enrichment (m is the number of terms in E_j). The terms 'regular' and 'enrichment' make reference to the fact that the 'regular' interpolation field is considered as the background field upon which the 'enrichment' is added. To avoid linear dependency, the order of any polynomial terms in the enrichment basis must be greater than the order of the partitions of unity φ_α. This is, however, not a sufficient condition [20]; algorithms to deal with the linear dependent case are described in [20].

Shape functions associated with (2) are termed GFEM shape functions. These shape functions are built from the product of a partition of unity φ_α and enrichment functions E_j:

$$\varphi_\alpha \times \{1, E_j\}. \tag{3}$$

In the GFEM, the partition of unity is in general provided by linear Lagrangian FEM shape functions. The partition of unity property of the functions φ_α implies that

$$\sum_{\alpha=1}^{N} \varphi_\alpha(\boldsymbol{x}) E_j(\boldsymbol{x}) = E_j(\boldsymbol{x}). \tag{4}$$

Consequently, any enrichment function E_j can be represented exactly through linear combinations of GFEM shape functions, and, if the enrichment functions E_j can approximate the solution of a boundary value problem, the corresponding GFEM shape functions also will.

In finite element notation, with an underlined symbol denoting a set of nodal quantities, the approximation for a vector field $\boldsymbol{q}(\boldsymbol{x})$ of order l over an a n-node enriched element, with all the nodes enriched, can be written as

$$\boldsymbol{q}_h(\boldsymbol{x}) = \underline{\boldsymbol{N}}\,(\boldsymbol{x})\,\underline{\hat{\boldsymbol{q}}} + \underline{\boldsymbol{N}}\,(\boldsymbol{x})\,\underline{\boldsymbol{N}}_E(\boldsymbol{x})\,\underline{\tilde{\boldsymbol{q}}}\,, \tag{5}$$

where $\underline{\boldsymbol{N}}$ is a $l \times (l \times n)$ matrix containing the standard finite element shape functions, $\underline{\boldsymbol{N}}_E$ is a $(l \times n) \times (l \times m \times n)$ matrix containing the extra basis terms for the enrichment, $\underline{\hat{\boldsymbol{q}}}$ is a $(l \times n) \times 1$ vector containing standard degrees of freedom and $\underline{\tilde{\boldsymbol{q}}}$ is a $(l \times m \times n) \times 1$ vector containing the extra degrees of freedom. The number of extra degrees of freedom per node is equal to the number of terms in the basis for the enrichment multiplied by the number of nodal unknowns. In standard finite elements, the matrix $\underline{\boldsymbol{N}}_E$ is empty. In the rest of the paper, we consider a two-dimensional configuration with nodal displacements as unknowns.

As noted in [18, 19], the approach of Equation (5) allows the enrichment to be performed from node to node in a mesh by activating the extra degrees of freedom $\underline{\tilde{\boldsymbol{q}}}$ when needed (a hierarchical finite element formulation based on the partition of unity method). For instance, in describing a displacement discontinuity, if the standard displacement field is interpolated by the regular interpolation $\underline{\boldsymbol{N}}\,\underline{\hat{\boldsymbol{q}}}$, the displacement jump, described by means of a difference in displacements in conventional interface finite elements, can be described through the enrichment $\underline{\boldsymbol{N}}\,\underline{\boldsymbol{N}}_E\,\underline{\tilde{\boldsymbol{q}}} = \mathcal{H}\,\underline{\boldsymbol{N}}\,\underline{\boldsymbol{H}}\,\underline{\tilde{\boldsymbol{q}}}$ [4], where $\mathcal{H}$ is the scalar valued Heaviside function ($m = 1$) and $\underline{\boldsymbol{H}}$ is a diagonal matrix identifying through a 1/0 switch which degrees of freedom to enrich ($\underline{\boldsymbol{H}}$ is the identity matrix if all the degrees of freedom of the element are enriched). This results in the $(l \times n) \times 1$ vector of extra degrees of freedom $\underline{\tilde{\boldsymbol{q}}}$ (same dimensions as the vector of standard degrees of freedom $\underline{\hat{\boldsymbol{q}}}$) and in the $(l \times n) \times (l \times n)$ matrix $\mathcal{H}\,\underline{\boldsymbol{H}}$. The enrichment concerns only nodes whose support is crossed by a discontinuity. For nodes whose support is not crossed by a discontinuity, the basis responsible for the enrichment is empty since the Heaviside function is a constant function over their supports and can be neglected. Since element stiffness matrices for elements with extra degrees of freedom are assembled only for active extra degrees of freedom, the standard matrix $\underline{\boldsymbol{N}}$ can be used in place of $\underline{\boldsymbol{N}}\,\underline{\boldsymbol{H}}$.

3. GFEM APPROXIMATION FOR POLYCRYSTALS

Consider a polycrystalline aggregate like the one shown in Figure 3. Let $\{\mathcal{G}_i\}_{i=1}^{N_\mathcal{G}}$ denote the set of all $N_\mathcal{G}$ grains (non-overlapping open sets) covering an open domain $\Omega \in \mathbb{R}^d$, $d = 2$ or 3. Therefore,

$$\bar{\Omega} = \bigcup_{i=1}^{N_\mathcal{G}} \bar{\mathcal{G}}_i. \tag{6}$$

Suppose now that the solution $\boldsymbol{u}$ of a boundary value problem defined on Ω is of the form

$$\boldsymbol{u} = \hat{\boldsymbol{u}} + \sum_{i=1}^{N_\mathcal{G}} \mathcal{H}_i \tilde{\boldsymbol{u}}_i, \tag{7}$$

where $\mathcal{H}_i(\boldsymbol{x})$ denotes a discontinuous function defined by

$$\mathcal{H}_i(\boldsymbol{x}) = \begin{cases} 1 & \text{if } \boldsymbol{x} \in \mathcal{G}_i \\ 0 & \text{otherwise} \end{cases}, \tag{8}$$

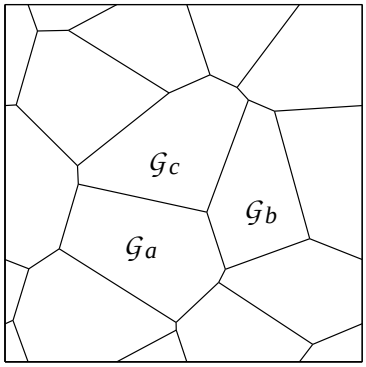

Figure 3. Polycrystalline aggregate.

while $\hat{\boldsymbol{u}}$ and $\tilde{\boldsymbol{u}}_i,\ i = 1, \ldots, N_{\mathcal{G}}$, are continuous functions defined on Ω and $\mathcal{G}_i$, respectively.

A piecewise linear approximation of $\boldsymbol{u}$ can be written using linear finite element shape functions, φ_α, defined on a background mesh as illustrated in Figure 2:

$$\begin{aligned} \boldsymbol{u}_h(\boldsymbol{x}) &= \hat{\boldsymbol{u}}_h(\boldsymbol{x}) + \sum_{i=1}^{N_{\mathcal{G}}} \mathcal{H}_i(\boldsymbol{x}) \tilde{\boldsymbol{u}}_{hi}(\boldsymbol{x}) \\ &= \sum_{\alpha=1}^{N} \varphi_\alpha(\boldsymbol{x})\, \underline{\hat{\boldsymbol{u}}}_\alpha + \sum_{i=1}^{N_{\mathcal{G}}} \sum_{\alpha=1}^{N} \mathcal{H}_i(\boldsymbol{x}) \varphi_\alpha(\boldsymbol{x})\, \underline{\tilde{\boldsymbol{u}}}_{\alpha i}, \end{aligned} \tag{9}$$

where N is the number of nodes in the finite element mesh and $\underline{\hat{\boldsymbol{u}}}_\alpha,\ \underline{\tilde{\boldsymbol{u}}}_{\alpha i},\ \alpha = 1, \ldots, N,\ i = 1, \ldots, N_{\mathcal{G}}$, are nodal degrees of freedom. The last equation can also be written as

$$\begin{aligned} \boldsymbol{u}_h(\boldsymbol{x}) &= \sum_{\alpha=1}^{N} \varphi_\alpha(\boldsymbol{x}) \left[\underline{\hat{\boldsymbol{u}}}_\alpha + \sum_{i=1}^{N_{\mathcal{G}}} \underline{\tilde{\boldsymbol{u}}}_{\alpha i} \mathcal{H}_i(\boldsymbol{x}) \right] \\ &= \sum_{\alpha=1}^{N} \varphi_\alpha(\boldsymbol{x}) \boldsymbol{u}_{h\alpha}(\boldsymbol{x}). \end{aligned} \tag{10}$$

Here, $\boldsymbol{u}_{h\alpha}$ represents a local approximation of $\boldsymbol{u}$ defined on the cloud ω_α, the support of the partition of unity function φ_α, [5, 6, 20–23]. The local approximations are linear combinations of enrichment functions

$$\{1, \mathcal{H}_1, \mathcal{H}_2, \ldots, \mathcal{H}_{N_{\mathcal{G}}}\}. \tag{11}$$

Comparing the above with (2), we have that

$$E_j(\boldsymbol{x}) = \mathcal{H}_j(\boldsymbol{x}) \qquad j = 1, \ldots, m = N_{\mathcal{G}}. \tag{12}$$

Equation (10) shows that the global approximation $\boldsymbol{u}_h(\boldsymbol{x})$ is build by pasting together local approximations $\boldsymbol{u}_{h\alpha}, \alpha = 1, \ldots, N$, using a partition of unity. This is a fundamental concept common to all partition of unity methods like the GFEM [5, 6, 17, 18, 21–23].

From (9)–(11), we have that at each node $\boldsymbol{x}_\alpha$ the following generalized FE shape functions are defined

$$\varphi_\alpha(\boldsymbol{x}) \times \{1, \mathcal{H}_1, \mathcal{H}_2, \ldots, \mathcal{H}_{N_{\mathcal{G}}}\} \tag{13}$$

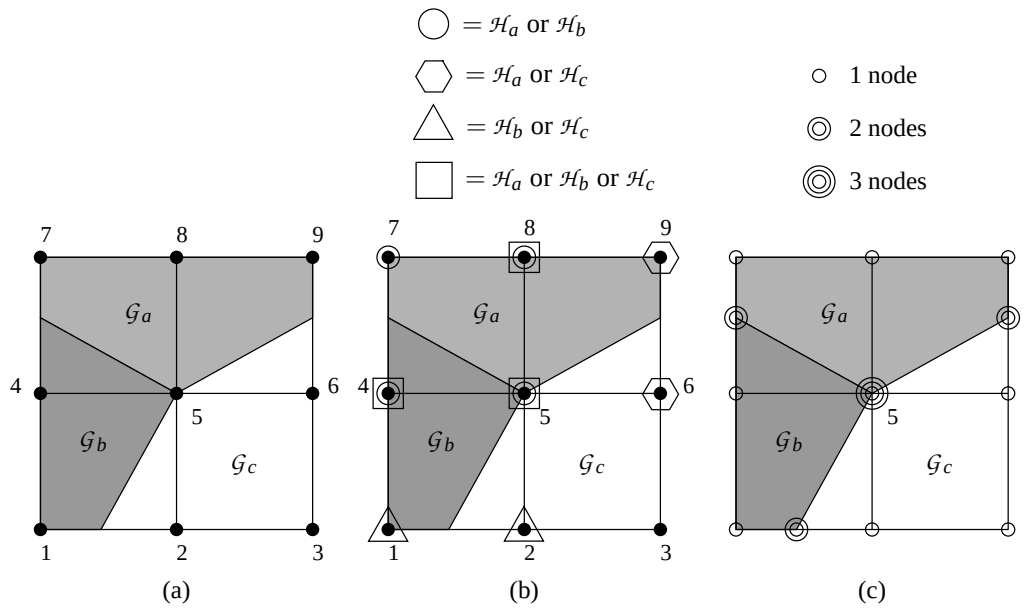

Figure 4. A triple junction with (a) grain boundaries not conforming to the mesh topology and (b) its corresponding GFEM discretization; (c) standard FEM discretization with explicit discontinuities along the grain boundaries.

which are built from the product of the finite element partition of unity and enrichment functions (11). However, in general, several step functions $\mathcal{H}_i$ are constant over the support ω_α of a given partition of unity function φ_α. In actual computations, only the enrichment functions that are non-constant over ω_α are used at node $\boldsymbol{x}_\alpha$.

Linear dependences of the *enrichment functions* must also be avoided. Let us consider, for example, the two-dimensional case illustrated in Figure 4a where, for the sake of the following considerations, the triple junction coincides with a node of the mesh, and examine the enrichment functions that must be used at each node of the mesh. The support ω_1 intersects $\partial\mathcal{G}_b$ and $\partial\mathcal{G}_c$. Therefore, the following shape functions could be used at node $\boldsymbol{x}_1$:

$$\varphi_1 \times \{1, \mathcal{H}_b, \mathcal{H}_c\}. \tag{14}$$

However, this set is linearly dependent since

$$\mathcal{H}_c = 1 - \mathcal{H}_b. \tag{15}$$

Therefore, either

$$\varphi_1 \times \{1, \mathcal{H}_b\} \quad \text{or} \quad \varphi_1 \times \{1, \mathcal{H}_c\} \tag{16}$$

should be used as shape functions at node $\boldsymbol{x}_1$.

Nodes $\boldsymbol{x}_2$, $\boldsymbol{x}_6$, $\boldsymbol{x}_7$, $\boldsymbol{x}_9$ can be treated using the same arguments. The support ω_3 of node $\boldsymbol{x}_3$ does not intersect any grain boundary and the only shape function associated with this node is the partition of unity φ_3. Consider now the case of node $\boldsymbol{x}_4$. The support ω_4 intersects $\partial\mathcal{G}_a$, $\partial\mathcal{G}_b$ and $\partial\mathcal{G}_c$. Therefore, the following shape functions could be used at node $\boldsymbol{x}_4$

$$\varphi_4 \times \{1, \mathcal{H}_a, \mathcal{H}_b, \mathcal{H}_c\}. \tag{17}$$

But again, this set is linearly dependent since

$$\mathcal{H}_c = 1 - \mathcal{H}_a - \mathcal{H}_b. \tag{18}$$

Therefore, at node $\boldsymbol{x}_4$, the following shape functions should be used instead:

$$\varphi_4 \times \{1, \mathcal{H}_a, \mathcal{H}_b\} \quad \text{or} \quad \varphi_4 \times \{1, \mathcal{H}_a, \mathcal{H}_c\} \quad \text{or} \quad \varphi_4 \times \{1, \mathcal{H}_b, \mathcal{H}_c\}. \tag{19}$$

The nodes $\boldsymbol{x}_5$ and $\boldsymbol{x}_8$ can be treated in a similar manner as node $\boldsymbol{x}_4$.

Figure 4b illustrates the resulting degrees of freedom at each node of the mesh. The discretization has a total of 40 degrees of freedom and can be written as

$$\begin{aligned} \boldsymbol{u}_h(\boldsymbol{x}) &= \varphi_1\{\underline{\hat{\boldsymbol{u}}}_1 + \underline{\tilde{\boldsymbol{u}}}_{1b}\mathcal{H}_b\} + \varphi_2\{\underline{\hat{\boldsymbol{u}}}_2 + \underline{\tilde{\boldsymbol{u}}}_{2b}\mathcal{H}_b\} + \varphi_3\{\underline{\hat{\boldsymbol{u}}}_3\} + \\ &\quad \varphi_4\{\underline{\hat{\boldsymbol{u}}}_4 + \underline{\tilde{\boldsymbol{u}}}_{4a}\mathcal{H}_a + \underline{\tilde{\boldsymbol{u}}}_{4b}\mathcal{H}_b\} + \varphi_5\{\underline{\hat{\boldsymbol{u}}}_5 + \underline{\tilde{\boldsymbol{u}}}_{5a}\mathcal{H}_a + \underline{\tilde{\boldsymbol{u}}}_{5b}\mathcal{H}_b\} + \\ &\quad \varphi_6\{\underline{\hat{\boldsymbol{u}}}_6 + \underline{\tilde{\boldsymbol{u}}}_{6a}\mathcal{H}_a\} + \varphi_7\{\underline{\hat{\boldsymbol{u}}}_7 + \underline{\tilde{\boldsymbol{u}}}_{7a}\mathcal{H}_a\} + \\ &\quad \varphi_8\{\underline{\hat{\boldsymbol{u}}}_8 + \underline{\tilde{\boldsymbol{u}}}_{8a}\mathcal{H}_a + \underline{\tilde{\boldsymbol{u}}}_{8b}\mathcal{H}_b\} + \varphi_9\{\underline{\hat{\boldsymbol{u}}}_9 + \underline{\tilde{\boldsymbol{u}}}_{9a}\mathcal{H}_a\} \\ &= \textstyle\sum_{\alpha=1}^{9} \varphi_\alpha \underline{\hat{\boldsymbol{u}}}_\alpha + \\ &\quad \mathcal{H}_a\left(\varphi_4 \underline{\tilde{\boldsymbol{u}}}_{4a} + \varphi_5 \underline{\tilde{\boldsymbol{u}}}_{5a} + \varphi_6 \underline{\tilde{\boldsymbol{u}}}_{6a} + \varphi_7 \underline{\tilde{\boldsymbol{u}}}_{7a} + \varphi_8 \underline{\tilde{\boldsymbol{u}}}_{8a} + \varphi_9 \underline{\tilde{\boldsymbol{u}}}_{9a}\right) + \\ &\quad \mathcal{H}_b\left(\varphi_1 \underline{\tilde{\boldsymbol{u}}}_{1b} + \varphi_2 \underline{\tilde{\boldsymbol{u}}}_{2b} + \varphi_4 \underline{\tilde{\boldsymbol{u}}}_{4b} + \varphi_5 \underline{\tilde{\boldsymbol{u}}}_{5b} + \varphi_8 \underline{\tilde{\boldsymbol{u}}}_{8b}\right). \end{aligned} \tag{20}$$

Other choices of enrichment functions are possible as discussed above.

Consider now the standard finite element discretization shown in Figure 4c composed of quadrilateral and triangular elements. It has a total of 34 degrees of freedom. However, if we consider the triangular elements as degenerated quadrilateral elements, the FE discretization would also have 40 degrees of freedom. The formulation presented here and a standard finite element mesh, in general, do not lead to the same discretization space. The same holds for the XFEM.

The choice of enrichment functions described above can be summarized as follows. Inside each local domain or cloud ω_α we take as enrichment functions the discontinuous functions $\mathcal{H}$ that are not identically constant over ω_α. If we have more than one enrichment function, one of them can be eliminated since it is a linear combination of the others and the constant function. This simple rule is valid for *any* grain topology and in any spacial dimension.

Higher order local enrichment functions can also be defined using this same approach. Extensions to three dimensions are conceptually identical but the computational implementation is, of course, more involved. The formulation described here can also be used for cases in which the junctions do not coincide with mesh nodes as illustrated in Section 6.2. In addition, the number of grain boundaries meeting at a point can be arbitrary.

4. GFEM EQUIVALENT DISCRETE SPACE

In what follows, we shall construct a discrete space for the mesh in Figure 5b by using discontinuous functions and show its equivalence to the discrete space related to the mesh in Figure 5a. In doing so, we parallel the derivations reported in [7]. To begin with, the finite element approximation associated with the mesh in Figure 5a reads

$$\boldsymbol{u}_h(\boldsymbol{x}) = \sum_{i \in I} \varphi_i \underline{\boldsymbol{u}}_i, \tag{21}$$

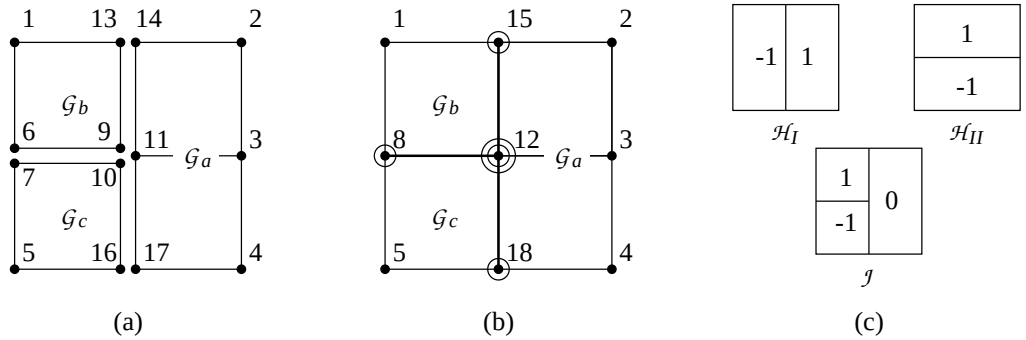

Figure 5. A triple junction can be modeled by (a) truly accounting for the three discontinuity lines or (b) by enriching nodes 8, 12, 15 and 18 with discontinuous functions (the black circles represent standard degrees of freedom while the white circles represent extra degrees of freedom). (c) XFEM enrichment functions [7].

where $I = \{1, 2, 3, 4, 5, 6, 7, 9, 10, 11, 13, 14, 16, 17\}$. The relation between the two meshes in Figure 5a and b can be established by defining nodal variables $\underline{\boldsymbol{\alpha}}$, $\underline{\boldsymbol{\beta}}$ and $\underline{\boldsymbol{\gamma}}$ as

$$\begin{array}{lll} \underline{\boldsymbol{\alpha}}_8 = \underline{\boldsymbol{u}}_6, & \underline{\boldsymbol{\gamma}}_8 = \underline{\boldsymbol{u}}_7 - \underline{\boldsymbol{u}}_6, & \\ \underline{\boldsymbol{\alpha}}_{12} = \underline{\boldsymbol{u}}_9, & \underline{\boldsymbol{\beta}}_{12} = \underline{\boldsymbol{u}}_{11} - \underline{\boldsymbol{u}}_9, & \underline{\boldsymbol{\gamma}}_{12} = \underline{\boldsymbol{u}}_{10} - \underline{\boldsymbol{u}}_9, \\ \underline{\boldsymbol{\alpha}}_{15} = \underline{\boldsymbol{u}}_{13}, & \underline{\boldsymbol{\beta}}_{15} = \underline{\boldsymbol{u}}_{14} - \underline{\boldsymbol{u}}_{13}, & \\ \underline{\boldsymbol{\alpha}}_{18} = \underline{\boldsymbol{u}}_{16}, & \underline{\boldsymbol{\beta}}_{18} = \underline{\boldsymbol{u}}_{17} - \underline{\boldsymbol{u}}_{16}. & \end{array} \tag{22}$$

With these definitions, we can express $\underline{\boldsymbol{u}}_i$ for $i = \{6, 7, 9, 10, 11, 13, 14, 16, 17\}$ as

$$\begin{array}{lll} \underline{\boldsymbol{u}}_6 = \underline{\boldsymbol{\alpha}}_8, & \underline{\boldsymbol{u}}_7 = \underline{\boldsymbol{\alpha}}_8 + \underline{\boldsymbol{\gamma}}_8, & \\ \underline{\boldsymbol{u}}_9 = \underline{\boldsymbol{\alpha}}_{12}, & \underline{\boldsymbol{u}}_{10} = \underline{\boldsymbol{\alpha}}_{12} + \underline{\boldsymbol{\gamma}}_{12}, & \underline{\boldsymbol{u}}_{11} = \underline{\boldsymbol{\alpha}}_{12} + \underline{\boldsymbol{\beta}}_{12}, \\ \underline{\boldsymbol{u}}_{13} = \underline{\boldsymbol{\alpha}}_{15}, & \underline{\boldsymbol{u}}_{14} = \underline{\boldsymbol{\alpha}}_{15} + \underline{\boldsymbol{\beta}}_{15}, & \\ \underline{\boldsymbol{u}}_{16} = \underline{\boldsymbol{\alpha}}_{18}, & \underline{\boldsymbol{u}}_{17} = \underline{\boldsymbol{\alpha}}_{18} + \underline{\boldsymbol{\beta}}_{18}. & \end{array} \tag{23}$$

By replacing these $\underline{\boldsymbol{u}}_i$ in (21) we find

$$\begin{aligned} \boldsymbol{u}_h(\boldsymbol{x}) &= \sum_{i \in I''} \varphi_i \, \underline{\boldsymbol{u}}_i + \varphi_6 \, \underline{\boldsymbol{\alpha}}_8 + \varphi_7 \left(\underline{\boldsymbol{\alpha}}_8 + \underline{\boldsymbol{\gamma}}_8 \right) + \varphi_9 \, \underline{\boldsymbol{\alpha}}_{12} + \varphi_{10} \left(\underline{\boldsymbol{\alpha}}_{12} + \underline{\boldsymbol{\gamma}}_{12} \right) + \varphi_{11} \left(\underline{\boldsymbol{\alpha}}_{12} + \underline{\boldsymbol{\beta}}_{12} \right) \\ &\quad + \varphi_{13} \, \underline{\boldsymbol{\alpha}}_{15} + \varphi_{14} \left(\underline{\boldsymbol{\alpha}}_{15} + \underline{\boldsymbol{\beta}}_{15} \right) + \varphi_{16} \, \underline{\boldsymbol{\alpha}}_{18} + \varphi_{17} \left(\underline{\boldsymbol{\alpha}}_{18} + \underline{\boldsymbol{\beta}}_{18} \right) \\ &= \sum_{i \in I''} \varphi_i \, \underline{\boldsymbol{u}}_i + (\varphi_6 + \varphi_7) \, \underline{\boldsymbol{\alpha}}_8 + \varphi_7 \underline{\boldsymbol{\gamma}}_8 + (\varphi_9 + \varphi_{10} + \varphi_{11}) \, \underline{\boldsymbol{\alpha}}_{12} + \varphi_{11} \underline{\boldsymbol{\beta}}_{12} \\ &\quad + \varphi_{10} \underline{\boldsymbol{\gamma}}_{12} + (\varphi_{13} + \varphi_{14}) \, \underline{\boldsymbol{\alpha}}_{15} + \varphi_{14} \underline{\boldsymbol{\beta}}_{15} + (\varphi_{16} + \varphi_{17}) \, \underline{\boldsymbol{\alpha}}_{18} + \varphi_{17} \underline{\boldsymbol{\beta}}_{18} \end{aligned} \tag{24}$$

with $I'' = \{1, 2, 3, 4, 5\}$. Considering Figure 5b and the linear combination of shape functions, we can replace $\varphi_6 + \varphi_7$, $\varphi_9 + \varphi_{10} + \varphi_{11}$, $\varphi_{13} + \varphi_{14}$ and $\varphi_{16} + \varphi_{17}$ by φ_8, φ_{12}, φ_{15} and φ_{18}, respectively and $\underline{\boldsymbol{\alpha}}_8$, $\underline{\boldsymbol{\alpha}}_{12}$, $\underline{\boldsymbol{\alpha}}_{15}$ and $\underline{\boldsymbol{\alpha}}_{18}$ by $\underline{\boldsymbol{u}}_8$, $\underline{\boldsymbol{u}}_{12}$, $\underline{\boldsymbol{u}}_{15}$ and $\underline{\boldsymbol{u}}_{18}$, respectively. Equation (24) can be now written as

$$\boldsymbol{u}_h(\boldsymbol{x}) = \sum_{i \in I'} \varphi_i \, \underline{\boldsymbol{u}}_i + \mathcal{H}_a \left(\varphi_{12} \underline{\boldsymbol{\beta}}_{12} + \varphi_{15} \underline{\boldsymbol{\beta}}_{15} + \varphi_{18} \underline{\boldsymbol{\beta}}_{18} \right) + \mathcal{H}_c \left(\varphi_8 \underline{\boldsymbol{\gamma}}_8 + \varphi_{12} \underline{\boldsymbol{\gamma}}_{12} \right) \tag{25}$$

with $I' = \{1, 2, 3, 4, 5, 8, 12, 15, 18\}$ the set of nodes in Figure 5b. The enrichment functions $\mathcal{H}$ are defined in Figure 5a by the junction topology ($\mathcal{H}_{a/c} = 1$ in $\mathcal{G}_{a/c}$). Equation (25) represents the discretized displacement field related to the choice of the nodal vectorial variables in (22) for the mesh depicted in Figure 5b. In the above derivations we made use of the notion of 'linear combination of shape functions' which is valid only away from the grain boundary since $\mathcal{H}$ is not defined on $\partial\mathcal{G}$.

Enrichment schemes different from the one given by (25) are of course possible, as long as the generated discrete spaces are equivalent to the reference discrete space related to the mesh depicted in Figure 5a. Indeed, using a different definition of the nodal vectorial variables in (22), Daux et al. [7] obtained (cf Equation (14) in [7])

$$\boldsymbol{u}_h(\boldsymbol{x}) = \sum_{i \in I'} \varphi_i \, \underline{\boldsymbol{u}}_i + \mathcal{H}_I \left(\varphi_{12} \, \underline{\boldsymbol{\beta}}_{12} + \varphi_{15} \, \underline{\boldsymbol{\beta}}_{15} + \varphi_{18} \, \underline{\boldsymbol{\beta}}_{18} \right) + \mathcal{H}_{II} \varphi_8 \, \underline{\boldsymbol{\beta}}_8 + \mathcal{J} \varphi_{12} \, \underline{\boldsymbol{\gamma}}_{12} \tag{26}$$

with the enrichments $\mathcal{H}_I$, $\mathcal{H}_{II}$ and $\mathcal{J}$ defined in Figure 5c.

With reference to Figure 5b, the counting of degrees of freedom equals 28 for both XFEM (Daux et al. [7]) and GFEM approximations. The standard FEM discretization shown in Figure 5a yields the same figure. Also, it is worth noting that the number of nodal enrichments is the same for XFEM and GFEM. Of course, this is not a proof of equivalence between discrete spaces spanned by the three approaches (FEM, XFEM and GFEM), but it shows, following [7], that the discrete spaces obtained by FEM, XFEM and GFEM are equivalent for a branched crack aligned with the mesh.

There is an important distinction with XFEM though. The approach devised in [7] defines a triple junction as the intersection of a main and a secondary discontinuity line. In our approach there is no need for such a distinction and all the enrichment functions are defined through the polycrystalline aggregate topology. There is no need for 'preprocessing' to define extra enrichment functions, a difficult task in a three-dimensional domain.

5. GFEM EQUATIONS

In this section, we summarize the governing equations and our assumptions. For the benefit of the reader, some of the definitions given in Section 3 are repeated. In the following, the range of the subscript i ($i = 1, \ldots, N_{\mathcal{G}}$) in $\mathcal{G}_i$ and related quantities is omitted when it is clear from the context.

5.1. Kinematics

Consider the polycrystalline aggregate $\bar{\Omega} = \Omega \cup \partial\Omega$ comprising $N_{\mathcal{G}}$ grains shown in Figure 6a (Ω is the set of all points inside the domain and $\partial\Omega$ is the set of boundary points which is decomposed into the part $\partial\Omega_u$ where displacements are prescribed and the complement $\partial\Omega_\sigma$ which has prescribed tractions). Denote with $\{\mathcal{G}_i\}$ the set of all grains covering the open domain Ω and let, for simplicity, a grain be defined as a set of connected straight-line grain boundary segments. Define $\partial\mathcal{G}_a$ as the boundary of grain $\mathcal{G}_a$ and, for a given adjacent grain $\mathcal{G}_b$, $\partial\mathcal{G}_{ab}$ is the boundary, belonging to grain $\mathcal{G}_a$, between grains $\mathcal{G}_a$ and $\mathcal{G}_b$, i.e.,

$$\partial\mathcal{G}_{ab} = \bar{\mathcal{G}}_a \cap \bar{\mathcal{G}}_b. \tag{27}$$

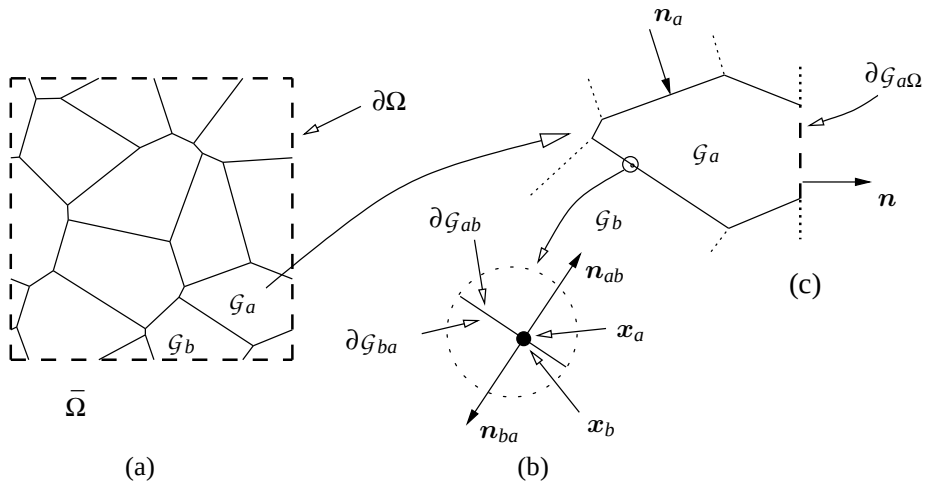

Figure 6. Nomenclature for the polycrystal sample.

The union of all grain faces of $\mathcal{G}_a$ shared with adjacent grains is denoted by $\mathcal{F}_a$:

$$\mathcal{F}_a = \bigcup_{i=1, i\neq a}^{N_\mathcal{G}} \partial\mathcal{G}_{ai} \tag{28}$$

The set $\mathcal{F}_a$ is depicted with a solid black line in Figure 6c. The union of the faces of grain $\mathcal{G}_a$ on the boundary $\partial\Omega$ is denoted by $\partial\mathcal{G}_{a\Omega}$. This set may be empty. It is not difficult to verify that

$$\partial\mathcal{G}_a = \mathcal{F}_a \cup \partial\mathcal{G}_{a\Omega} \tag{29}$$

and that

$$\mathcal{F}_a \cap \partial\mathcal{G}_{a\Omega} = \emptyset. \tag{30}$$

Let $\boldsymbol{n}_a$ be the set of inward unit normal vectors to the boundary $\mathcal{F}_a$ of grain $\mathcal{G}_a$. Further, grain boundary segments are given in a counter-clock-wise sense such that the normals $\boldsymbol{n}_a$ to grain boundary $\mathcal{F}_a$ point inward to the grain domain.

Here, for simplicity we consider small strains and displacements. The extension to large deformation problems will be the subject of a subsequent paper. Following the derivations of Section 3, the displacement field $\boldsymbol{u}$ is defined by

$$\boldsymbol{u}(\boldsymbol{x}) = \hat{\boldsymbol{u}}(\boldsymbol{x}) + \sum_{i=1}^{N_\mathcal{G}} \mathcal{H}_i(\boldsymbol{x})\, \tilde{\boldsymbol{u}}_i(\boldsymbol{x}), \tag{31}$$

where $\hat{\boldsymbol{u}}$ and $\tilde{\boldsymbol{u}}_i$ are continuous functions and the discontinuous function $\mathcal{H}_i$ is defined in (8). Consequently, the strain field $\boldsymbol{\varepsilon}$ within the grains, away from grain boundaries and junctions, is defined by

$$\boldsymbol{\varepsilon}(\boldsymbol{x}) = \boldsymbol{\nabla}_\mathrm{s}\hat{\boldsymbol{u}}(\boldsymbol{x}) + \sum_{i=1}^{N_\mathcal{G}} \mathcal{H}_i \boldsymbol{\nabla}_\mathrm{s}\tilde{\boldsymbol{u}}_i(\boldsymbol{x}) = \hat{\boldsymbol{\varepsilon}}(\boldsymbol{x}) + \sum_{i=1}^{N_\mathcal{G}} \mathcal{H}_i(\boldsymbol{x})\, \tilde{\boldsymbol{\varepsilon}}_i(\boldsymbol{x}), \tag{32}$$

where $\boldsymbol{\nabla}_{\mathrm{s}}$ is the symmetric part of the gradient operator.

The only relevant kinematic quantity at a grain boundary is the displacement jump. With reference to Figure 6b-c, the displacement jump across the boundary between grains a and b is defined as

$$[\![\boldsymbol{u}]\!]_{ab}(\boldsymbol{x}) = \boldsymbol{u}(\boldsymbol{x}_a) - \boldsymbol{u}(\boldsymbol{x}_b) = \tilde{\boldsymbol{u}}_a(\boldsymbol{x}) - \tilde{\boldsymbol{u}}_b(\boldsymbol{x}) \tag{33}$$

where a point $\boldsymbol{x}$ on the grain boundary is denoted $\boldsymbol{x}_a$ (or $\boldsymbol{x}_b$) if the grain boundary belongs to grain a (or b). It is also convenient to define $[\![\boldsymbol{u}]\!]_a$ as the set of the displacement jumps across the grain boundaries $\mathcal{F}_a$.

5.2. Strong form of the governing equations

Our objective is to define the governing equations for small displacement linear elasticity with linear cohesive discontinuities.

The point of departure is the strong form of the equilibrium equations without body forces,

$$\nabla \cdot \boldsymbol{\sigma} = \mathbf{0} \text{ in } \Omega, \tag{34}$$

and Hooke's law

$$\boldsymbol{\sigma} = \boldsymbol{C} : \boldsymbol{\varepsilon}, \tag{35}$$

with $\boldsymbol{C}$ the elasticity tensor. To complete the set of governing equations, we impose the boundary conditions

$$\boldsymbol{u} = \boldsymbol{u}^0 \text{ on } \partial\Omega_u \quad \text{and} \quad \boldsymbol{\sigma}\boldsymbol{n} = \boldsymbol{t}^0 \text{ on } \partial\Omega_\sigma, \tag{36}$$

where $\boldsymbol{n}$ is the outward unit normal vector to $\partial\Omega$ and $\boldsymbol{t}^0$ and $\boldsymbol{u}^0$ are prescribed tractions and displacements, respectively. Further, we require

$$\boldsymbol{\sigma}\boldsymbol{n}_i = \boldsymbol{t}_i \text{ on } \mathcal{F}_i \tag{37}$$

at grain boundaries of each grain i. We consider a traction-separation constitutive law of the type

$$\boldsymbol{t}_i = \boldsymbol{T}_i [\![\boldsymbol{u}]\!]_i, \tag{38}$$

where the definition of $\boldsymbol{t}_i$ and $\boldsymbol{T}_i$ parallels that of $[\![\boldsymbol{u}]\!]_i$. With reference to Figure 6b-c and considering grains a and b, the traction at the boundary $\partial\mathcal{G}_{ab}$ is defined by $\boldsymbol{t}_{ba}\,(= -\boldsymbol{t}_{ab})$ and, in a local frame of reference aligned with $\partial\mathcal{G}_{ab}$, the second-order constitutive tensor $\boldsymbol{T}_{ab}$ is assumed to be defined as

$$[\boldsymbol{T}_{ab}]_{ns} = [\boldsymbol{T}_{ba}]_{ns} = \begin{bmatrix} d_{nn} & d_{ns} \\ d_{sn} & d_{ss} \end{bmatrix}, \tag{39}$$

where the subscripts n and s stand for normal and tangential direction, respectively.

5.3. Weak form of the governing equations

The weak form of the governing equations is obtained after multiplication of the equilibrium equations (34) by the virtual displacement field $\boldsymbol{w}$ which has the same form as the displacement field (31):

$$\int_\Omega \hat{\boldsymbol{w}} \cdot (\nabla \cdot \boldsymbol{\sigma})\, \mathrm{d}v + \sum_{i=1}^{N_\mathcal{G}} \int_{\mathcal{G}_i} \tilde{\boldsymbol{w}}_i \cdot (\nabla \cdot \boldsymbol{\sigma})\, \mathrm{d}v = 0. \tag{40}$$

From the decomposition of the displacement field, it follows that any admissible variation $\boldsymbol{w}$ of $\boldsymbol{u}$ can be regarded as admissible variations $\hat{\boldsymbol{w}}$ and $\tilde{\boldsymbol{w}}_i$ thus leading to $N_{\mathcal{G}}+1$ weak variational statements, namely,

$$\int_{\Omega} \hat{\boldsymbol{w}} \cdot (\nabla \cdot \boldsymbol{\sigma}) \, \mathrm{d}v = 0, \tag{41a}$$

$$\int_{\mathcal{G}_i} \tilde{\boldsymbol{w}}_i \cdot (\nabla \cdot \boldsymbol{\sigma}) \, \mathrm{d}v = 0. \tag{41b}$$

Using standard algebraic relationships, the divergence theorem, the strain definition (32) and the stress–strain relationship (35), the $N_{\mathcal{G}}+1$ variational statements (41) become

$$\int_{\Omega} \hat{\boldsymbol{\varepsilon}} : \boldsymbol{C} : \boldsymbol{\varepsilon} \, \mathrm{d}v = \int_{\partial\Omega} \boldsymbol{\sigma}\hat{\boldsymbol{w}} \cdot \boldsymbol{n} \, \mathrm{d}s, \tag{42a}$$

$$\int_{\mathcal{G}_i} \tilde{\boldsymbol{\varepsilon}}_i : \boldsymbol{C} : \boldsymbol{\varepsilon} \, \mathrm{d}v + \int_{\mathcal{F}_i} \boldsymbol{\sigma}\tilde{\boldsymbol{w}}_i \cdot \boldsymbol{n}_i \, \mathrm{d}s = \int_{\partial\mathcal{G}_{i\Omega}} \boldsymbol{\sigma}\tilde{\boldsymbol{w}}_i \cdot \boldsymbol{n} \, \mathrm{d}s. \tag{42b}$$

The second integral in the LHS of (42b) is the sum of all contributions from grain boundaries belonging to grain $\mathcal{G}_i$ that are not on the boundary $\partial\Omega$, i.e. internal grain boundaries. Considering the relation (37) for the tractions across grain boundaries and the definition (33) of the displacement jump, it can be expressed as

$$\begin{aligned} \int_{\mathcal{F}_i} \boldsymbol{\sigma}\tilde{\boldsymbol{w}}_i \cdot \boldsymbol{n}_i \, \mathrm{d}s = \int_{\mathcal{F}_i} \tilde{\boldsymbol{w}}_i \cdot \boldsymbol{\sigma}\boldsymbol{n}_i \, \mathrm{d}s = \int_{\mathcal{F}_i} \tilde{\boldsymbol{w}}_i \cdot \boldsymbol{t}_i \, \mathrm{d}s \\ = \sum_j \int_{\partial\mathcal{G}_{ij}} \tilde{\boldsymbol{w}}_i \cdot \boldsymbol{T}_{ij} [\![\boldsymbol{u}]\!]_{ij} \, \mathrm{d}s = \sum_j \int_{\partial\mathcal{G}_{ij}} \tilde{\boldsymbol{w}}_i \cdot \boldsymbol{T}_{ij} \left(\tilde{\boldsymbol{u}}_i - \tilde{\boldsymbol{u}}_j\right) \, \mathrm{d}s. \end{aligned} \tag{43}$$

The last term of (43) can be simplified by considering that $\partial\mathcal{G}_{i\Omega} = \partial\mathcal{G}_{i\Omega u} \cup \partial\mathcal{G}_{i\Omega\sigma}$ with $\partial\mathcal{G}_{i\Omega u} \cap \partial\mathcal{G}_{i\Omega\sigma} = \emptyset$ and that, consistent with the individual-variations argument used to derive (41), $\tilde{\boldsymbol{w}}_i = \boldsymbol{0}$ on $\partial\mathcal{G}_{i\Omega u}$ $(i = 1, \ldots, N_{\mathcal{G}})$. With the above simplifications at hand, the weak form of the governing equations can be finally stated as

$$\int_{\Omega} \hat{\boldsymbol{\varepsilon}} : \boldsymbol{C} : \boldsymbol{\varepsilon} \, \mathrm{d}v = \int_{\partial\Omega_\sigma} \hat{\boldsymbol{w}} \cdot \boldsymbol{t}^0 \, \mathrm{d}s, \tag{44a}$$

$$\int_{\mathcal{G}_i} \tilde{\boldsymbol{\varepsilon}}_i : \boldsymbol{C} : \boldsymbol{\varepsilon} \, \mathrm{d}v + \sum_j \int_{\partial\mathcal{G}_{ij}} \tilde{\boldsymbol{w}}_i \cdot \boldsymbol{T}_{ij} \left(\tilde{\boldsymbol{u}}_i - \tilde{\boldsymbol{u}}_j\right) \, \mathrm{d}s = \int_{\partial\mathcal{G}_{i\Omega\sigma}} \tilde{\boldsymbol{w}}_i \cdot \boldsymbol{t}^0 \, \mathrm{d}s \quad (i = 1, \ldots, N_{\mathcal{G}}). \tag{44b}$$

When there are no extra degrees of freedom $\tilde{\boldsymbol{u}}$ activated in an element, $\boldsymbol{u} = \hat{\boldsymbol{u}}$ and (44a) is the only valid variational statement: the standard equilibrium equations are recovered.

5.4. Finite element discretization

We define the discretized kinematics and specialize the discretized equilibrium equations to a simple case. We use a Bubnov-Galerkin approach in which variations of the displacement field are interpolated as the displacement field.

The discretized displacement field (9) can be written using standard matrix notation as

$$\boldsymbol{u}_h = \underline{\boldsymbol{N}} \, \underline{\hat{\boldsymbol{u}}} + \sum_{i=1}^{N_{\mathcal{G}}} \mathcal{H}_i \, \underline{\boldsymbol{N}} \, \underline{\tilde{\boldsymbol{u}}}_i, \tag{45}$$

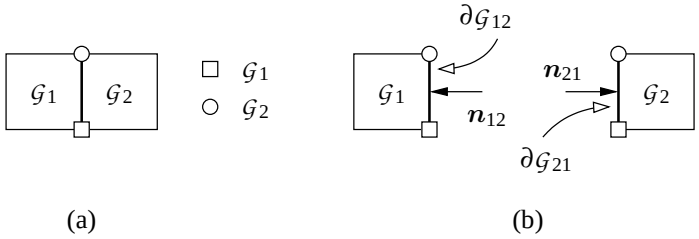

Figure 7. Two-grain polycrystal: (a) nodal enrichment and choice of extra degrees of freedom; (b) element-wise enrichment.

where $\underline{\boldsymbol{N}}$ is a matrix containing the usual finite element shape functions, and the vectors $\underline{\hat{\boldsymbol{u}}}$ and $\underline{\tilde{\boldsymbol{u}}}_i$, containing nodal quantities, are defined as $\underline{\hat{\boldsymbol{u}}} = \{\underline{\hat{\boldsymbol{u}}}_\alpha\}_{\alpha=1}^{N}$ and $\underline{\tilde{\boldsymbol{u}}}_i = \{\underline{\tilde{\boldsymbol{u}}}_{\alpha i}\}_{\alpha=1}^{N}$ (see (9)). Accordingly, the strain field (32) is discretized as

$$\boldsymbol{\varepsilon} = \underline{\boldsymbol{B}}\,\underline{\hat{\boldsymbol{u}}} + \sum_{i=1}^{N_{\mathcal{G}}} \mathcal{H}_i\,\underline{\boldsymbol{B}}\,\underline{\tilde{\boldsymbol{u}}}_i, \tag{46}$$

where $\underline{\boldsymbol{B}}$ is a matrix containing spatial derivatives of the shape functions. Finally, the displacement jump (33) across the boundary between grains i and j is discretized as

$$[\![\boldsymbol{u}]\!]_{ij} = \underline{\boldsymbol{N}}\,(\underline{\tilde{\boldsymbol{u}}}_i - \underline{\tilde{\boldsymbol{u}}}_j)\,. \tag{47}$$

As noted in Section 2, the arrays $\underline{\boldsymbol{N}}$ multiplying $\underline{\hat{\boldsymbol{u}}}_i$ and $\underline{\tilde{\boldsymbol{u}}}_j$ are normally not the same since only part of the extra degrees of freedom in the array $\underline{\tilde{\boldsymbol{u}}}$ might be activated (a similar argument holds for $\underline{\boldsymbol{B}}$). However, since the resulting element stiffness matrices are assembled only for active extra degrees of freedom, it is still possible, and convenient from an implementation point of view, to use the standard $\underline{\boldsymbol{N}}$ and $\underline{\boldsymbol{B}}$ arrays. The added computational cost is negligible, since only relatively few elements are usually enriched.

These discretized kinematic quantities are substituted into the weak form (44) and yield a discretized set of equilibrium equations. The derivations are a trivial algebraic exercise. However, it is illuminating to report the stiffness matrix related to the governing equations for the two-grain polycrystal depicted in Figure 7 in which the grain boundary lies between element (i.e. grain) $\mathcal{G}_1$ and $\mathcal{G}_2$:

$$\underline{\boldsymbol{K}}_{\mathcal{G}} = \begin{bmatrix} \underline{\boldsymbol{K}} & \underline{\boldsymbol{K}}_1 & \underline{\boldsymbol{K}}_2 \\ \underline{\boldsymbol{K}}_1 & \underline{\boldsymbol{K}}_1 + \underline{\boldsymbol{K}}_{12} & -\underline{\boldsymbol{K}}_{12} \\ \underline{\boldsymbol{K}}_2 & -\underline{\boldsymbol{K}}_{21} & \underline{\boldsymbol{K}}_2 + \underline{\boldsymbol{K}}_{21} \end{bmatrix}, \tag{48}$$

where the submatrices are

$$\underline{\boldsymbol{K}} = \int_{\Omega} \underline{\boldsymbol{B}}^{\mathrm{T}}\,\underline{\boldsymbol{C}}\,\underline{\boldsymbol{B}}\,\mathrm{d}v \tag{49a}$$

$$\underline{\boldsymbol{K}}_1 = \int_{\mathcal{G}_1} \underline{\boldsymbol{B}}^{\mathrm{T}}\,\underline{\boldsymbol{C}}\,\underline{\boldsymbol{B}}\,\mathrm{d}v \tag{49b}$$

$$\underline{\boldsymbol{K}}_2 = \int_{\mathcal{G}_2} \underline{\boldsymbol{B}}^{\mathrm{T}}\,\underline{\boldsymbol{C}}\,\underline{\boldsymbol{B}}\,\mathrm{d}v \tag{49c}$$

$$\underline{\boldsymbol{K}}_{12} = \int_{\partial\mathcal{G}_{12}} \underline{\boldsymbol{N}}^{\mathrm{T}}\, \underline{\boldsymbol{T}}\, \underline{\boldsymbol{N}}\, \mathrm{d}s \tag{49d}$$

$$\underline{\boldsymbol{K}}_{21} = \int_{\partial\mathcal{G}_{21}} \underline{\boldsymbol{N}}^{\mathrm{T}}\, \underline{\boldsymbol{T}}\, \underline{\boldsymbol{N}}\, \mathrm{d}s \tag{49e}$$

with $\underline{\boldsymbol{T}}_{12} = \underline{\boldsymbol{T}}_{21} = \underline{\boldsymbol{T}}$. Here, $\underline{\boldsymbol{C}}$ and $\underline{\boldsymbol{T}}$ are the matrix equivalent of the associated tensors $\boldsymbol{C}$ and $\boldsymbol{T}$, respectively. In the general case, the symmetry of the global system of equations derives from the symmetry of the tensors $\boldsymbol{C}$ and $\boldsymbol{T}$; by considering symmetric tensors $\boldsymbol{C}$ and $\boldsymbol{T}$, the global stiffness matrix is symmetric since $\underline{\boldsymbol{K}}_{12}$ and $\underline{\boldsymbol{K}}_{21}$ are surface integrals along the same grain boundary segment with the same integrand.

The element stiffness matrices for element $\mathcal{G}_1$ and $\mathcal{G}_2$ are obtained by specializing (48) to each of the two grains and considering the element-wise enrichment shown in Figure 7b:

$$\underline{\boldsymbol{K}}_{\mathcal{G}_1} = \begin{bmatrix} \underline{\boldsymbol{K}} & \underline{\boldsymbol{K}}_1 & \mathbf{0} \\ \underline{\boldsymbol{K}}_1 & \underline{\boldsymbol{K}}_1 + \underline{\boldsymbol{K}}_{12} & -\underline{\boldsymbol{K}}_{12} \\ \mathbf{0} & \mathbf{0} & \mathbf{0} \end{bmatrix}, \tag{50}$$

$$\underline{\boldsymbol{K}}_{\mathcal{G}_2} = \begin{bmatrix} \underline{\boldsymbol{K}} & \mathbf{0} & \underline{\boldsymbol{K}}_2 \\ \mathbf{0} & \mathbf{0} & \mathbf{0} \\ \underline{\boldsymbol{K}}_2 & -\underline{\boldsymbol{K}}_{21} & \underline{\boldsymbol{K}}_2 + \underline{\boldsymbol{K}}_{21} \end{bmatrix}. \tag{51}$$

In this particular case, the individual element stiffness matrices are not symmetric, but their assembly is.

Although the case just presented is very simple, the structure of (48), due to the particular choice of the nodal enrichment, is very similar to that encountered in the discretization of a polycrystal with only triple junctions. In that case, only two extra degrees of freedom per node per junction suffice as will be explained in Section 6.2.

6. FINITE ELEMENT IMPLEMENTATION

In the following, some issues pertinent to the implementation of the proposed method are outlined.

The numerical integration of element arrays deriving from the weak form (44) for elements with a grain boundary or a junction requires trivial, although somehow intricate, modifications to standard element integration schemes [4, 7]. Although there are no restrictions on element type, we have used four-node bilinear quadrilateral continuum finite elements, and have triangulated each of the domains resulting from elements with a grain boundary or a junction as depicted in Figure 8. In each of the triangles we have used a 3-point integration scheme. For integration along grain boundaries we have used a 2-point Gauss integration scheme. A standard 2×2 Gauss integration scheme has been used in the remaining elements. Other procedures are described in [24–26].

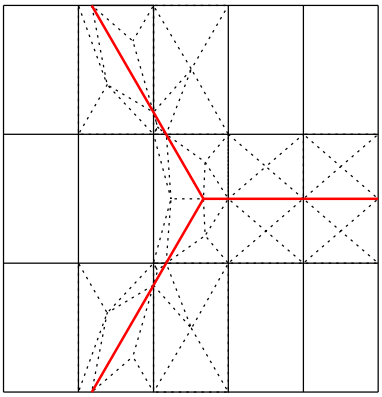

Figure 8. Close-up of 15 quadrilateral elements around a triple junction (grain boundaries in red). Note the triangulated subpolygons used in the element quadrature routines.

6.1. Enforcement of essential boundary conditions

When a node on the sample boundary has one or more extra degrees of freedom as a consequence of the GFEM enrichment discussed in Section 3, essential boundary conditions must be enforced with some precautions. Indeed, standard techniques cannot be used to directly impose boundary conditions on enriched nodes, and, in general, the Kronecker-delta interpolation properties of the basis are not fulfilled at a generic location along the boundary of an element crossed by a discontinuity line.

Consider, for simplicity, the linear quadrilateral element shown in Figure 9 in the parent element space, and suppose that side $\overline{ab}$ is part of the boundary along which a prescribed value $\boldsymbol{u}^0$ of $\boldsymbol{u} = \hat{\boldsymbol{u}} + \mathcal{H}\tilde{\boldsymbol{u}}$ is prescribed. Enforcement of $\boldsymbol{u}^0$ along side $\overline{ab}$ results in the following constraint equations:

$$\hat{\boldsymbol{u}}_a = \boldsymbol{u}^0 \quad \text{at vertex } a, \tag{52a}$$

$$\hat{\boldsymbol{u}}_b + \tilde{\boldsymbol{u}}_b = \boldsymbol{u}^0 \quad \text{at vertex } b, \tag{52b}$$

$$N_a\hat{\boldsymbol{u}}_a + N_b\hat{\boldsymbol{u}}_b = \boldsymbol{u}^0 \quad \text{at point } p\,(\mathcal{H} = 0)\,, \tag{52c}$$

$$N_a\hat{\boldsymbol{u}}_a + N_a\tilde{\boldsymbol{u}}_a + N_b\hat{\boldsymbol{u}}_b + N_b\tilde{\boldsymbol{u}}_b = \boldsymbol{u}^0 \quad \text{at point } p\,(\mathcal{H} = 1)\,, \tag{52d}$$

where the shape functions N_a and N_b are evaluated at p.

The constraints on essential boundary conditions are enforced by a penalty method [27]. By using this approach, penalty energy terms enter the variational form. Penalty stiffnesses and force vectors are derived by making use of the concept of Courant quadratic penalty function [28, 29]; these terms are assembled like standard element contributions to the global system of equations. As other approaches, see e.g. [30, 31], are equally feasible, we have preferred not to make the variational form depending on a specific method, and therefore we have not incorporated penalty terms in the variational form.

6.2. A simple automated procedure for GFEM nodal enrichment

Nodal enrichment is performed in two steps. First, any node whose support is intersected by a grain boundary is enriched by the corresponding $\mathcal{H}$ function, as shown in Figure 10a. This is

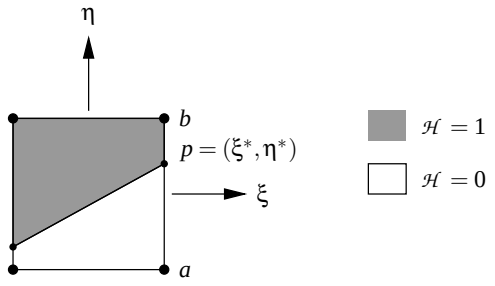

Figure 9. Schematic for constraint equations in parent element space.

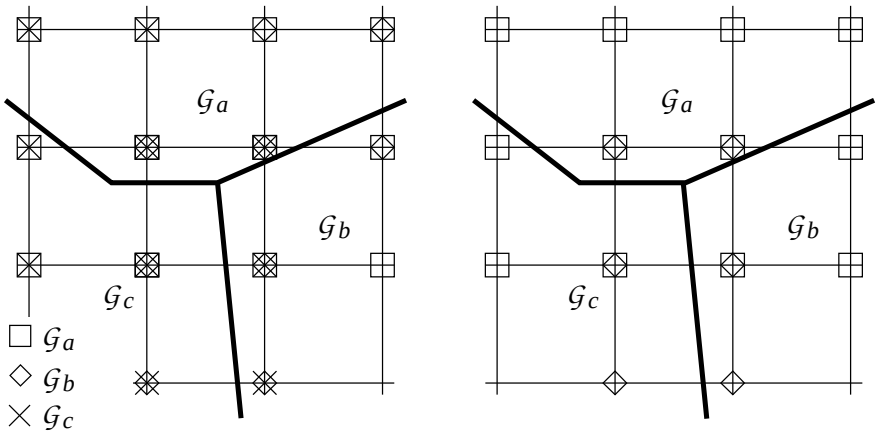

Figure 10. Nodal enrichment procedure for polycrystalline aggregates: (a) grain enrichment functions are added to all grains; (b) surplus enrichment functions are eliminated.

done for each grain following standard techniques [4] (at this stage, nodes that do not pass the area test, as proposed in [32], are not enriched). Next, a loop is done on all enriched nodes and the last added enrichment function is removed unless only one enrichment function would be left (Figure 10b). Such a procedure results in an enrichment scheme coherent with the GFEM enrichment scheme presented in Section 3. As a side remark, a polycrystalline aggregate with only triple junctions has at most two different enrichment functions per node (provided that the mesh resolution is fine enough to have neighboring junctions separated by more than one element).

As already pointed out in Section 4, our approach results in an easier, and more general, choice of the enrichment scheme than the one proposed by Daux et al. [7] (compare our enrichment scheme, reported in Figure 10b with the one according to Daux et al. [7] reported in Figure 11).

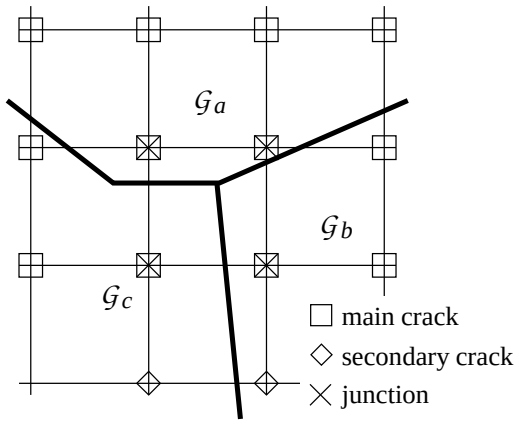

Figure 11. XFEM enrichment scheme for a grain junction (adapted from [7]).

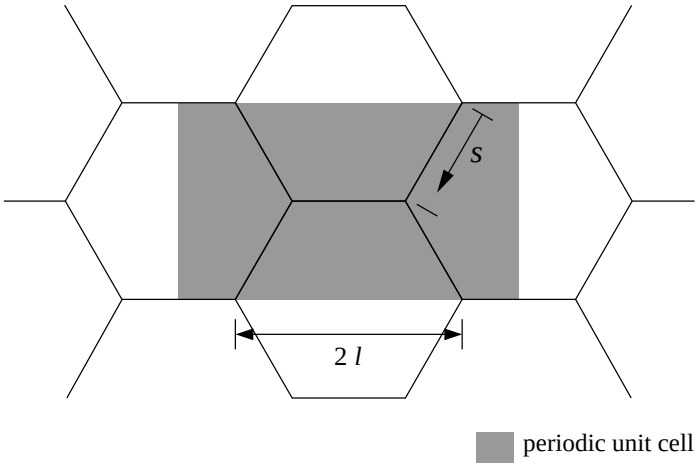

Figure 12. Schematic of the periodic unit cell used in the example. s is the local coordinate along GB facets of length l.

7. FREE GRAIN BOUNDARY SLIDING AND ANELASTICITY OF POLYCRYSTALS

Under appropriate loading conditions and temperature, grain boundary sliding is one of the main mechanisms behind anelastic deformation of polycrystalline aggregates. One of the limiting cases of grain boundary-driven deformation is when grain boundaries can freely slide against each other. This so-called 'relaxed state' occurs at sufficiently low strain rates when the viscous resistance of grain boundaries can be neglected. A body in the relaxed state has a lower rigidity than the unrelaxed one in which shear tractions are transmitted across the grain boundaries. Many micromechanical studies have attempted to give an analytical estimate of the relaxed mechanical properties of polycrystalline aggregates. Amongst them we recall: (Z)

the self consistent method by Zener [33], in which grains are considered as sliding circular inclusions in a matrix with the same stiffness; the self-consistent method by Budiansky and Hill [34, 35] (SC) and Mori and Tanaka [36] (MT), in which grains are modeled as sliding circular inclusions (analytical expressions for the effective moduli are reported in [37]); (CB) the self consistent method by O'Connell and Budiansky [38], in which grain boundaries are described by randomly oriented flat shear cracks filled with viscous fluid; and (DSC) the microcrack model by Fotiu and Heuer [39], in which grain boundaries are modeled as a dilute distribution of shear cracks.

Some numerical analyses have confuted the validity of the above micromechanical studies by showing that a valid estimate must rely on an accurate representation of the stress field in the polycrystalline aggregate and, above all, must take into account the kinematic constraints imposed by grain junctions. To the authors' knowledge, the first of these numerical studies in elastic polycrystals is due to Ghahremani [14], who characterized the role of grain boundary sliding in a periodic arrangement of hexagonal grains. Subsequent studies concentrated on the effect of grain boundary sliding on the creeping behavior of polycrystals [13, 40], and on the effect of microstructural variations on steady state creep and facet stresses in freely sliding polycrystals [41].

In this section, we study the effect of free grain boundary sliding on anelasticity of polycrystals [14] to demonstrate the abilities of our GFEM scheme. The polycrystal is modeled as a periodic arrangement of hexagonal grains. The representative unit cell shown in Figure 12 has been discretized by means of a structured background mesh of linear quadrilateral elements. The enforcement of the periodic boundary conditions described in Appendix I is done according to the derivations reported in Section 6.1. We obtained a good compromise constraint-enforcement versus stability of the system for a penalty weight of 10^4 times the largest term in the global stiffness matrix. Each grain is isotropically elastic in a plane strain configuration. Free sliding along grain boundaries is assumed and, to avoid penetration (and separation) of adjacent grains, the stiffness in the normal direction across grain boundaries has been given a high value. With reference to (39), $d_{ss} = 0$, $d_{sn} = d_{ns} = 0$ and $d_{nn} = 10^4 E/l$, where E is the Young's modulus of the grains and l is the length of the grain boundary $\partial\mathcal{G}$ between two adjacent grains (see Figure 12). The relaxed Young modulus $\bar{E}$ is computed as the ratio of the relaxed stress $\bar{\sigma}$ to the applied strain ε. The relaxed stress $\bar{\sigma}$ $(= \bar{\sigma}_{11})$ is defined by the sum of the reaction forces in the horizontal direction along the right-hand side of the periodic unit cell divided by the vertical cross sectional area (i.e. the length of the right-hand side of the periodic unit cell times 1); the sum of the vertical reaction forces along the same side is zero. The applied strain ε is defined as the ratio of the prescribed displacement to the length of the horizontal side.

The ratio $\bar{E}/E$ of the relaxed to the unrelaxed Young's modulus as a function of the Poisson's ratio reported in Figure 13 for two discretizations (squares and circles) shows an excellent agreement with the reference numerical results obtained in [14]. Results from the estimates previously described are also reported. A good agreement with the reference solution [14] was found even with one of the coarsest discretizations used in this study (Ghahremani [14] used 1512 constant strain triangular elements in our GFEM unit cell with mesh refinement along grain boundaries (i.e. 756 elements/grain); we have used $28 \times 19 = 532$ linear quadrilateral elements ($\circ$) in the GFEM unit cell with a uniform grid). The profile of the displacement jump in the tangential direction depicted in Figure 14 shows a rapid convergence, thus indicating that a dense discretization (like e.g. the 147×49 element grid) might not be necessary for

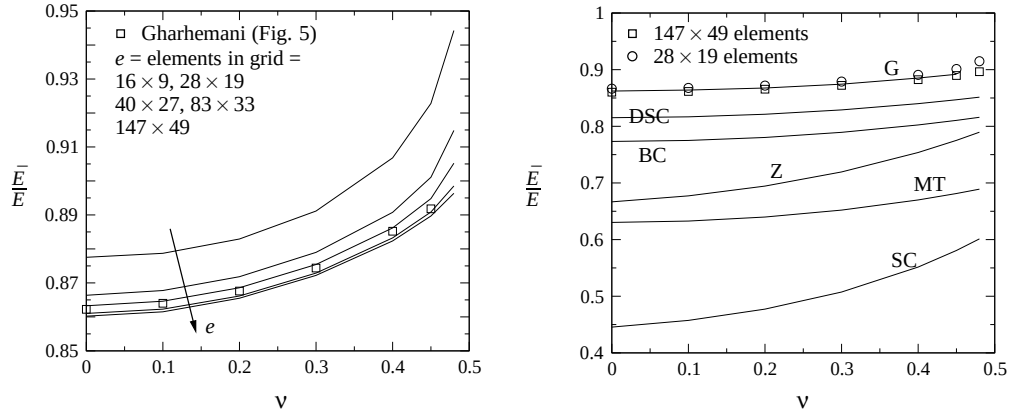

Figure 13. The ratio $\bar{E}/E$ vs ν: effect of mesh refinement (left) and comparison with results from the literature (right; Ghahremani [14] (G), Fotiu and Heuer [39] (DSC), O'Connell and Budiansky [38] (BC), Zener [33] (Z), Mori and Tanaka [36] (MT), Budiansky and Hill [34, 35] (SC)).

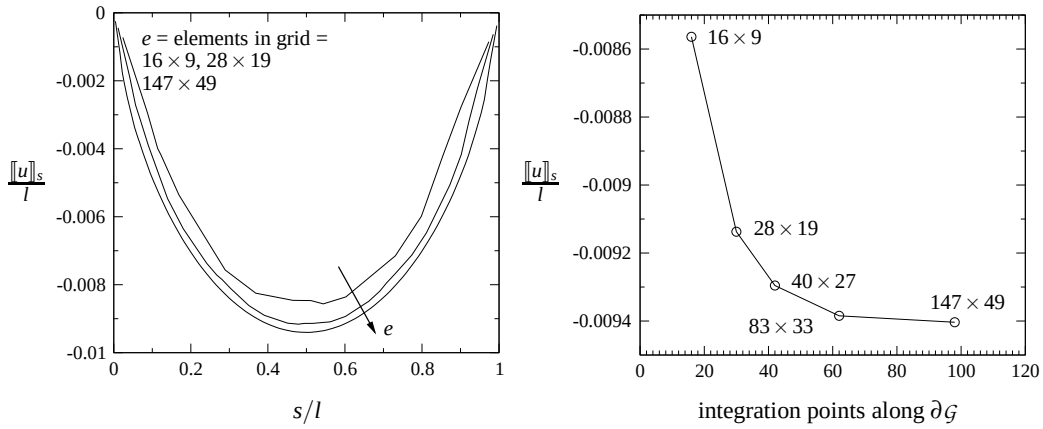

Figure 14. Displacement jump in the tangential direction along an inclined grain boundary ($\nu = 0.3$): effect of mesh refinement on global profile (left) and on the value at the center, $s/l = 0.5$ (right).

practical purposes.

A close-up of the zone around a grain boundary, for $s/l \approx 0.5$ is shown in Figure 15. Recall that the domain is discretized by means of quadrilateral elements; the triangular sub-domains shown are used only in element quadrature routines (cf Section 6). Finally, the distribution of the ratio of the von Mises stress σ_e to the overall applied equivalent stress $\bar{\sigma}_e = \bar{\sigma}_{11}$ is shown in Figure 16.

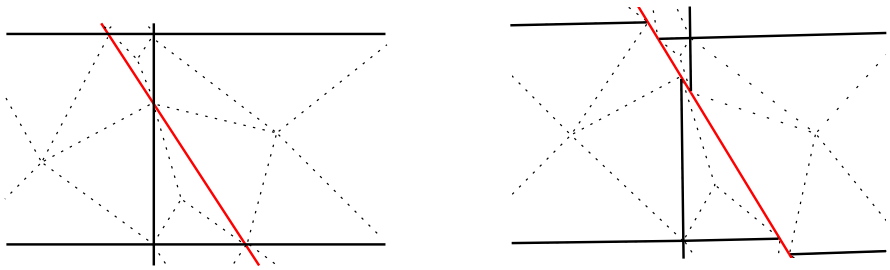

Figure 15. Close-up of the mesh around a grain boundary for $s/l \approx 0.5$ (grain boundary in red, quadrilateral element boundaries in solid black, triangular sub-domains for element quadrature routines in dotted black): undeformed (left) and deformed configuration (right) for a 40×27 element grid mesh.

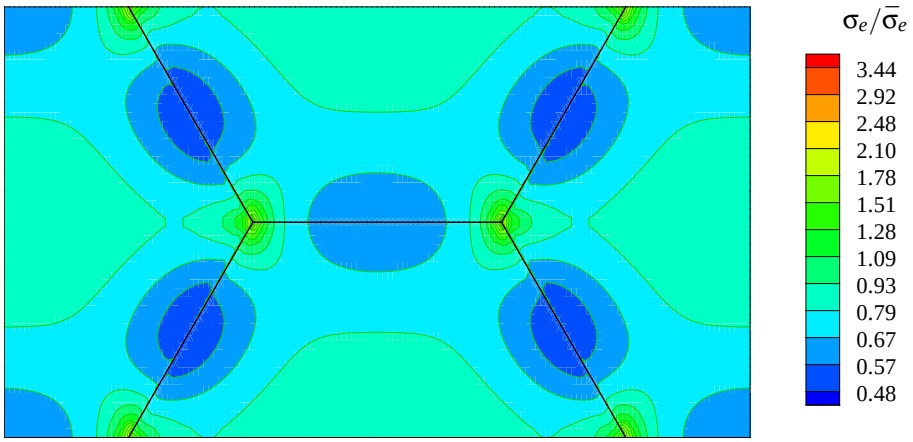

Figure 16. Contour plot of the ratio of the von Mises stress σ_e to the overall applied equivalent stress $\bar{\sigma}_e = \bar{\sigma}_{11}$ (147×49 element grid; $\nu = 0.3$). The effect of full relaxation of the shear stresses along the grain boundaries is a strong redistribution of the internal stress state, leading to enhanced strains and hence a reduced modulus. A detail of the mesh around the triple junction is shown in Figure 8

8. SUMMARY AND CONCLUDING REMARKS

In this work we have proposed a Generalized Finite Element Method for polycrystals in which the finite element mesh does not need to conform to the polycrystal microstructure. We have customized the discontinuous enrichment proposed in [4] and made it apt to describe grain boundaries and junctions. The enrichment scheme proposed in Section 3 represents the main improvement over the approach by Daux's et al. [7]. Indeed, our approach to junction

enrichments generalizes their approach in two dimensions, extends it to three dimensions and makes the implementation more straightforward since we are free to choose among several enrichment possibilities at a given node. Although the focus in deriving the enrichment scheme was on the description of grain junctions, problems involving crack propagation, interaction and coalescence [42, 43] can benefit from our approach.

The application to grain boundary sliding in Section 7 showed that, as in standard finite element methods, the quality of the GFEM approximation depends on the level of refinement of the background mesh. Alternatively, the GFEM approximation can also be improved through p-type enrichment of the approximation spaces defined on a course background mesh [18, 19].

Finally, it is worth noting that in recent years there has been a proliferation of methods [30] based on the partition of unity approach which was proposed independently by Babuška and colleagues [6, 21, 22] (under the names "special finite element methods", "generalized finite element method" and "partition of unity finite element method") and by Duarte and Oden [5, 17, 18, 23] (under the names "*hp* clouds" and "cloud-based *hp* finite element method"). The only distinctive characteristic is the choice of the basis functions. Additional methods based on the partition of unity approach are, for example, [4, 44–46]. Indeed, the distinction between the XFEM [4, 7] and the proposed GFEM for polycrystals is somehow immaterial in the sense that both approaches relies on the definition of a partition of unity and on the use of the approximation (5) with a discontinuous enrichment. Only the choice of the enrichment scheme differentiates the XFEM formulation proposed by Daux et al. [7] from the proposed GFEM for polycrystals. What sets our approach apart is the simplicity with which we can deal with any number of branches, the selection of enrichment functions, and the extension to three dimensions and to higher order approximations.

ACKNOWLEDGMENTS

The support of this work by the Netherlands Institute for Metals Research (NIMR) under Project No. MC4.02128 (A. Simone) and by The University of Illinois at Urbana-Champaign (C.A. Duarte) is gratefully acknowledged.

REFERENCES

[1] Sukumar N, Srolovitz DJ, Baker TJ, Prévost JH. Brittle fracture in polycrystalline microstructures with the extended finite element method. *International Journal for Numerical Methods in Engineering* 2003; **56**:2015–2037.

[2] Kuprat A, George D, Straub G, Demirel MC. Modeling microstructure evolution in three dimensions with Grain3D and LaGriT. *Computational Materials Science* 2003; **28**:199–208.

[3] Weyer S, Fröhlich A, Riesch-Oppermann H, Cizelj L, Kovac M. Automatic finite element meshing of planar Voronoi tessellations. *Engineering Fracture Mechanics* 2002; **69**:945–958.

[4] Moës N, Dolbow J, Belytschko T. A finite element method for crack growth without

remeshing. *International Journal for Numerical Methods in Engineering* 1999; **46**(1):131–150.

[5] Duarte CAM, Oden JT. *Hp* clouds—an *hp* meshless method. *Numerical Methods for Partial Differential Equations* 1996; **12**:673–705.

[6] Melenk JM, Babuška I. The partition of unity finite element method: Basic theory and applications. *Computer Methods in Applied Mechanics and Engineering* 1996; **139**:289–314.

[7] Daux C, Moës N, Dolbow J, Sukumar N, Belytschko T. Arbitrary branched and intersecting cracks with the extended finite element method. *International Journal for Numerical Methods in Engineering* 2000; **48**:1741–1760.

[8] Wells GN, Sluys LJ. A new method for modelling cohesive cracks using finite elements. *International Journal for Numerical Methods in Engineering* 2001; **50**(12):2667–2682.

[9] Moës N, Belytschko T. Extended finite element method for cohesive crack growth. *Engineering Fracture Mechanics* 2002; **69**:813–833.

[10] Van der Giessen E, Tvergaard V. A creep-rupture model accounting for cavitation at sliding grain-boundaries. *International Journal of Fracture* 1991; **48**(3):153–178.

[11] Bower AF, Wininger E. A two-dimensional finite element method for simulating the constitutive response and microstructure of polycrystals during high temperature plastic deformation. *Journal of the Mechanics and Physics of Solids* 2004; **52**:1289–1317.

[12] Chen JS, Kotta V, Lu H, Wang D, Moldovan D, Wolf D. A variational formulation and a double-grid method for meso-scale modelling of stressed grain growth in polycrystalline materials. *Computer Methods in Applied Mechanics and Engineering* 2004; **193**:1277–1303.

[13] Crossman FW, Ashby MF. The non-uniform flow of polycrystals by grain-boundary sliding accommodated by power-law creep. *Acta Metallurgica* 1975; **23**:425–440.

[14] Ghahremani F. Effect of grain boundary sliding on anelasticity of polycrystals. *International Journal of Solids and Structures* 1980; **16**:825–845.

[15] Ghosh S, Moorthy S. Elastic-plastic analysis of arbitrary heterogeneous materials with the Voronoi cell finite-element method. *Computer Methods in Applied Mechanics and Engineering* 1995; **121**(1–4):373–409.

[16] Sukumar N, Tabarraei A. Conforming polygonal finite elements. *International Journal for Numerical Methods in Engineering* 2004; **61**:2045–2066.

[17] Oden JT, Duarte CA. Clouds, cracks and FEM's. In Reddy BD (ed.), *Recent Developments in Computational and Applied Mechanics*. International Center for Numerical Methods in Engineering, CIMNE, Barcelona, Spain, 1997; 302–321.

[18] Oden JT, Duarte CA, Zienkiewicz OC. A new cloud-based *hp* finite element method. *Computer Methods in Applied Mechanics and Engineering* 1998; **153**:117–126.

[19] Taylor RL, Zienkiewicz OC, Oñate E. A hierarchical finite element method based on the partition of unity. *Computer Methods in Applied Mechanics and Engineering* 1998; **152**(1–2):73–84.

[20] Duarte CA, Babuška I, Oden JT. Generalized finite element methods for three dimensional structural mechanics problems. *Computers and Structures* 2000; **77**:215–232.

[21] Babuška I, Caloz G, Osborn JE. Special finite element methods for a class of second order elliptic problems with rough coefficients. *SIAM Journal on Numerical Analysis* 1994; **31**(4):945–981.

[22] Babuška I, Melenk JM. The partition of unity finite element method. *International Journal for Numerical Methods in Engineering* 1997; **40**:727–758.

[23] Duarte CAM, Oden JT. An *hp* adaptive method using clouds. *Computer Methods in Applied Mechanics and Engineering* 1996; **139**:237–262.

[24] Espelid TO, Genz A. DECUHR: An algorithm for automatic integration of singular functions over a hyper-rectangular region. *Numerical Algorithms* 1994; **8**:201–220.

[25] Strouboulis T, Babuška I, Copps K. The design and analysis of the generalized finite element method. *Computer Methods in Applied Mechanics and Engineering* 2000; **181**:43–96.

[26] Duarte CA, Hamzeh ON, Liszka TJ, W W. A generalized finite element method for the simulation of three-dimensional dynamic crack propagation. *Computer Methods in Applied Mechanics and Engineering* 2001; **190**:2227–2262.

[27] Chessa J, Smolinski P, Belytschko T. The extended finite element method (XFEM) for solidification problems. *International Journal for Numerical Methods in Engineering* 2002; **53**:1957–1977.

[28] Belytschko T, Liu WK, Moran B. *Nonlinear Finite Elements for Continua and Structures*. John Wiley & Sons, Chichester, England, 2000.

[29] Felippa CA. Introduction to Finite Element Methods (ASEN 5007). Course notes. Department of Aerospace Engineering Sciences, University of Colorado at Boulder, USA, 2004.

[30] Babuška I, Banerjee U, Osborn JE. Survey of meshless and generalized finite element methods: A unified approach. *Acta Numerica* 2003; **12**:1–125.

[31] Ji H, Dolbow JE. On strategies for enforcing interfacial constraints and evaluating jump conditions with the extended finite element method. *International Journal for Numerical Methods in Engineering* 2004; **61**:2508–2535.

[32] Dolbow J, Moës N, Belytschko T. Discontinuous enrichment in finite elements with a partition of unity method. *Finite Elements in Analysis and Design* 2000; **36**:235–260.

[33] Zener C. *Elasticity and Anelasticity of Metals*. The University of Chicago Press, Chicago, 1948.

[34] Budiansky B. On the elastic moduli of some heterogeneous materials. *Journal of the Mechanics and Physics of Solids* 1965; **13**:223–227.

[35] Hill R. A self-consistent mechanics of composite materials. *Journal of the Mechanics and Physics of Solids* 1965; **13**:213–222.

[36] Mori T, Tanaka K. Average stress in matrix and average elastic energy of materials with misfitting inclusions. *Acta Metallurgica* 1973; **21**:571–574.

[37] Jun S, Jasiuk I. Elastic moduli of two-dimensional composites with sliding inclusions - A comparison of effective medium theories. *International Journal of Solids and Structures* 1993; **30**(18):2501–2523.

[38] O'Connell RJ, Budiansky B. Viscoelastic properties of fluid-saturated cracked solids. *Journal of Geophysical Research* 1977; **82**:5719–5736.

[39] Fotiu PA, Heuer R. Overall stiffness of an elastic polycrystal with relaxed grain boundaries. *Zeitschrift fur Angewandte Mathematik und Mechanik* 1997; **77**(S2):S465–S468.

[40] Ghahremani F. Effect of grain boundary sliding on steady creep of polycrystals. *International Journal of Solids and Structures* 1980; **16**:847–862.

[41] Onck P, Van der Giessen E. Influence of microstructural variations on steady state creep and facet stresses in 2-D freely sliding polycrystals. *International Journal of Solids and Structures* 1997; **34**(6):703–726.

[42] Remmers JJC, de Borst R, Needleman A. A cohesive segments method for the simulation of crack growth. *Computational Mechanics* 2003; **31**(1–2):69–77.

[43] Zi G, Song JH, Budyn E, Lee SH, Belytschko T. A method for growing multiple cracks without remeshing and its application to fatigue crack growth. *Modelling and Simulations in Materials Science and Engineering* 2004; **12**:901–915.

[44] De S, Bathe KJ. The method of finite spheres with improved numerical integration. *Computers and Structures* 2001; **79**:2183–2196.

[45] Griebel M, Schweitzer MA. A Particle-Partition of Unity Method for the solution of elliptic, parabolic and hyperbolic PDE. *SIAM Journal on Scientific Computing* 2000; **22**(3):853–890.

[46] Strouboulis T, Copps K, Babuška I. The generalized finite element method. *Computer Methods in Applied Mechanics and Engineering* 2001; **190**:4081–4193.

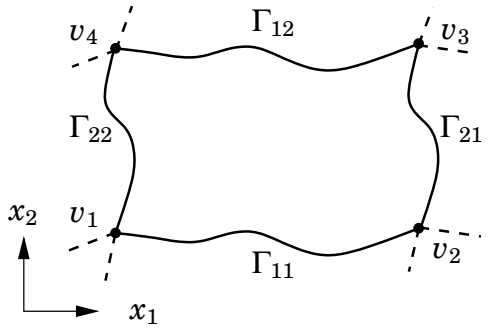

Figure 17. Schematic of a periodic unit cell with nomenclature for periodic boundary conditions.

APPENDIX

I. PERIODIC BOUNDARY CONDITIONS

With reference to the periodic unit cell depicted in Figure 17, uniaxial tensile loading conditions are specified by letting $\boldsymbol{u}^0_{v_2} = (u^0, 0)^{\mathrm{T}}$, with u^0 the prescribed displacement in the horizontal direction. Further, vertex v_1 is constrained in both directions to prevent rigid body motion, vertex v_3 is tied to the other nodes by the vertex constraint equations, and vertex v_4 is free ($\boldsymbol{u}_{v_i}$ is the displacement for vertex v_i). Displacement boundary conditions specialized for tensile loading along the x_1 direction, read as follows:

$$\boldsymbol{u}_{12} - \boldsymbol{u}_{11} = \boldsymbol{u}_{v_4} \quad \text{(top-bottom constraint)}, \tag{53a}$$

$$\boldsymbol{u}_{21} - \boldsymbol{u}_{22} = \boldsymbol{u}^0_{v_2} \quad \text{(left-right constraint)}, \tag{53b}$$

$$\boldsymbol{u}_{v_3} - \boldsymbol{u}_{v_4} = \boldsymbol{u}^0_{v_2} \quad \text{(vertex constraint)}, \tag{53c}$$

where $\boldsymbol{u}_{ij}$ is the displacement for any point, vertices excluded, on the corresponding boundary Γ_{ij}.